

Preparation and Electrosorption Desalination Performance of Peanut Shell-Based Activated Carbon and MoS₂

Bole Pan¹, Yaqi Wang², Haibo Li³, Wei Yi², Yongzhang Pan^{2,}*

¹ Guangzhou Tianhe Foreign Language School, Guangzhou 510627, China

² School of Environment, Jinan University, Guangzhou 511443, China

³ School of Chemistry, Sun Yat-Sen University, Guangzhou 510275, China

*E-mail: tpyz@jnu.edu.cn

Received: 4 August 2019/ *Accepted:* 30 September 2019 / *Published:* 31 December 2019

Seawater desalination is an unavoidable path to solve the freshwater crisis. Compared with other methods, hybrid capacitive deionization (HCDI) is considered promising, showing competence in efficiency and cost. In this study, activated carbon based on peanut shells and molybdenum disulfide (MoS₂) was prepared using a hydrothermal method, and the as-prepared products were subjected to heat treatment for more effective charge transfer. The synthesized materials were characterized using X-ray diffraction (XRD), scanning electron microscopy (SEM), transmission electron microscopy (TEM), and energy dispersive spectrometry (EDS), along with Raman spectra analysis and electrochemical workstation and BET analyses. The electrodes demonstrated outstanding HCDI performance, with an electrosorption capacity of 8.98 mg/g. The above result was attributed to the large pore width of the peanut shell-based activated carbon and the decreased resistance of the MoS₂. Moreover, the possibility of using solar power as a power source for HCDI is proven during tests, promoting the application of the study for portable seawater desalination in arid coastal and island regions worldwide.

Keywords: Capacitive deionization; peanut shell; activated carbon; MoS₂; solar power

1. INTRODUCTION

Four billion people are facing severe water scarcity, accounting for more than 50% of the global population [1]. As seawater and brackish water make up approximately 97.4% of the total amount of water [2], it is evident that seawater desalination is an inevitable path for tackling the water crisis. Traditional desalination methods include reverse osmosis, distillation, and electrodialysis. Of all the various methods, reverse osmosis (RO) accounts for 65% of the world's installed desalination capacity [3]. However, seawater desalination has not been universally adopted for the production of drinking water at a commercial scale due to its high energy consumption [4-7]. In the last few years, the research

communities and industries have turned their attention to the method of capacitive deionization (CDI) for its application in seawater desalination due to its main advantages: low energy consumption, low environmental impact, and low operating cost compared to those of other technologies [8-12].

CDI technology is limited to the processing of slightly or moderately concentrated NaCl solutions, such as brackish water, [13-15] due to co-ion expulsion or counter-ion adsorption at the interface of the electrode. Two main ideas are considered to improve the performance of the CDI reactor for application in seawater desalination: one is to improve the performance of CDI electrodes, and the other is to modify the reactor configuration. In regard to improving the CDI electrodes, their desalination performances are affected by the pore pattern and size distribution of carbon materials. Researchers have suggested that mesoporous carbon electrodes had a higher electrosorption capacity than common activated carbon electrodes [16]. Modifications of composite surface properties can significantly enhance the performance of electrodes. AC/ZrO₂ nanocomposites were fabricated to improve the wettability and specific capacitance of CDI electrodes [17]. After titania was used to chemically modify activated carbon (AC), higher salt adsorption capacities and better cycling stability could be reached [10]. Ar plasma-modified Ti₃C₂T_x was used as an electrode material to increase the efficiency of sodium-ion transport, and a removal capacity of 26.8 mg g⁻¹ was obtained under an external power of 1.2 V [18]. With regard to configuration modifications, features such as membrane capacitive deionization (MCDI) could increase the desalination rate [19-22]; the introduced ion-exchange membranes could directly restrict co-ions from accessing the electrodes, while the counter-ions could be easily adsorbed by the electrodes, and thus, the salt removal efficiency would increase [23].

This work aims to increase the electrosorption capacity by enhancing the performance of electrode materials. Activated carbon is the conventional material for the preparation of CDI electrodes due to its high specific surface area, good electronic conductivity, stability, and mature production techniques [24-26]. However, as the cost of producing activated carbon increases, the recycling of biomass wastes for the synthesis of activated carbon is becoming more attractive both economically and environmentally [27-32]. As one of the main waste biomass materials, peanut shells have been used as carbon sources for preparing activated carbon, and this has been attracting great attention because of their low ash content, low apparent density, and high degree of porosity [33-37]. Peanut is a crop with drought tolerance capability, worldwide distribution, and great annual yield, with approximately 6 million tons of peanut shell waste generated in the world during 2010 [38]. Using peanut shell waste to prepare activated carbon can not only be environmentally friendly but also reduce the cost of producing activated carbon [39]. Moreover, MoS₂ has been applied as a material for desalination [40,41] because the weak van der Waals interactions between the S-Mo-S layers allow easy intercalation of electrolyte ions in the material [42-44].

This research introduces AC/MoS₂ hybrid electrodes for the desalination of seawater. The waste peanut shell was selected as a precursor to prepare low-cost AC, and the MoS₂ sample experienced thermal treatment for more effective charge transfer inside the MoS₂. By comparing the untreated MoS₂ electrode to the heat-treated MoS₂ electrode, we reveal the effects of the defect on the electrode material performance to remove salt. This study also provides new insight into the desalination of seawater by AC prepared from agricultural wastes.

2. EXPERIMENTAL

2.1. Materials and reagents

All the reagents used in these experiments were of analytical grade. Sodium molybdate (Na_2MoO_4), thiourea ($\text{CN}_2\text{H}_4\text{S}$), sodium chloride (NaCl), potassium hydroxide (KOH), acetylene black, carbamide ($\text{CH}_4\text{N}_2\text{O}$) and N-methyl pyrrolidone ($\text{C}_5\text{H}_9\text{NO}$) used in this study were purchased from Damao Chemical Reagent Co., Ltd. (Tianjin, China). Polyvinylidene difluoride (PVDF) was purchased from Arkema Kynar Co., Ltd. (France). All solutions were prepared with ultrapure water from a Milli-Q system.

2.2. Methods

2.2.1 Preparation of peanut shell-based activated carbon

Activated carbon was prepared based on peanut shells. A schematic illustration of activated carbon is shown in Figure 1. Peanut shells were washed, torn into pieces, and dried under sunlight for 48 hours. The pretreated shells were then put into crucibles that were in turn placed into a SX2-4-10A (Huyueming Co. Ltd. Shanghai, China) muffle furnace and carbonized at 450 °C for 2 hours. The samples were washed and dried at 60 °C for 8 hours to obtain peanut shell-based carbon materials. The materials were then ground into powder and mixed with potassium hydroxide (KOH) and carbamide ($\text{CH}_4\text{N}_2\text{O}$) in a weight ratio of 1:2:1. The mixed powder was stirred and soaked in deionized water for 24 hours. After washing and drying, it was calcined in nitrogen flow for 3 hours at 750 °C. The product was washed with a solution of hydrochloric acid and deionized water and then dried. The peanut shell-based activated carbon obtained in this study is named PS-AC for brevity.



Figure 1. Schematic fabrication for the activated carbon.

2.2.2 Preparation of molybdenum disulfide

Molybdenum disulfide was synthesized by a one-step hydrothermal method. Sodium molybdate (0.5 g $\text{Na}_2\text{MoO}_4 \cdot 2\text{H}_2\text{O}$) and thiourea (0.7 g $\text{CN}_2\text{H}_4\text{S}$) were dissolved in 90 mL deionized water. The solution was vigorously stirred for 30 minutes to form a homogeneous solution and then ultrasonicated for 15 minutes. Then, the mixture was transferred into a 100-mL Teflon-lined stainless-steel autoclave. It was kept at 180 °C for 24 hours. After cooling, it was filtered and washed twice with deionized water and ethanol and dried at 60 °C for 8 hours to obtain molybdenum disulfide (named untreated MoS_2). The sample was subjected to thermal treatment at 300 °C for 2 hours in the muffle furnace to introduce defects, followed by washing of the as-prepared sample with deionized water for the removal of oxides. The thermally treated sample was named D- MoS_2 in this study (Figure 2).

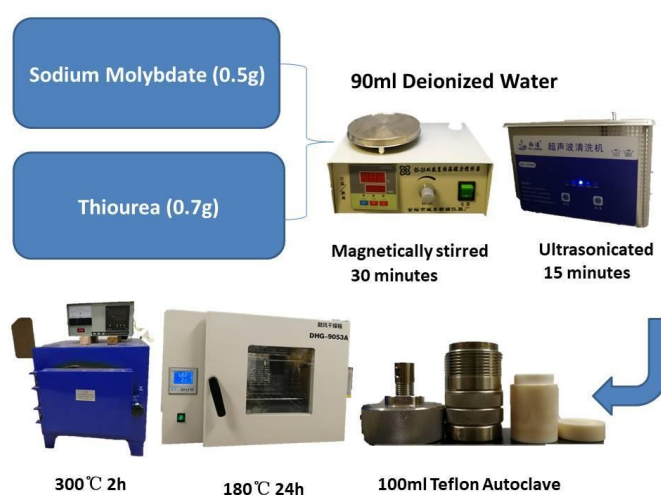


Figure 2. Schematic fabrication of MoS_2 and subsequent thermal treatment.

2.2.3 Preparation of electrodes

The PS-AC electrode was prepared by mixing pretreated PS-AC powder, polyvinylidene difluoride (PVDF) and acetylene black in a weight ratio of 8:1:1. N-methyl pyrrolidone was added to the mixed powder, and the mixture was magnetically stirred for 3 hours and then ultrasonicated for 1 hour at room temperature to form a homogeneous solution. The mixture was dried in the furnace at 60 °C until it thickened and was then applied to 6 cm x 8 cm nickel foams. The PS-AC electrodes were obtained by drying for 8 hours before being pressed by a press machine and dried for another 4 hours. D- MoS_2 electrodes were prepared following the same method as that of the PS-AC electrodes, only replacing PS-AC with D- MoS_2 . For comparison, a commercial activated carbon for supercapacitors (SC-AC) from XINSEN Co. (Fujian, China) was applied to fabricate the electrode. To eliminate the ions introduced during preparation, all prepared electrodes were washed with deionized water and then dried before desalination experiments (Figure 3).

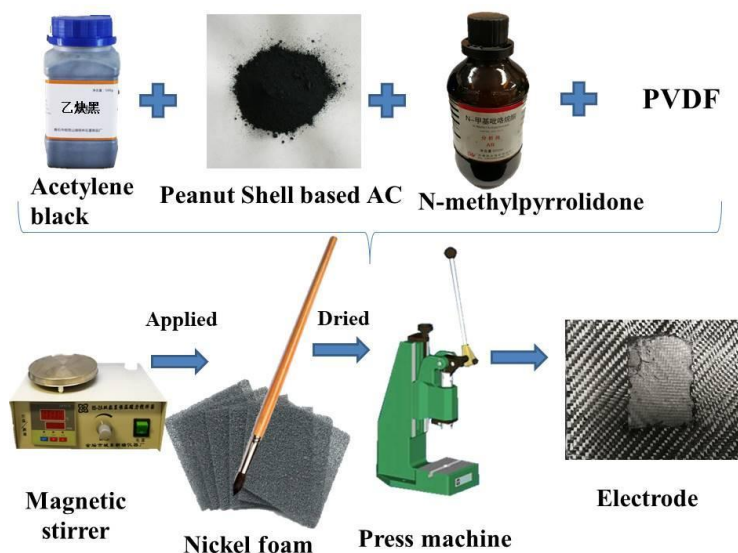


Figure 3. Schematic preparation of electrodes.

2.3 Characterization

The morphologies of the samples were characterized with a scanning electron microscope (SEM, JSM-6701F Quanta 400FEG) and an X-ray energy dispersive spectroscope (EDS). The Brunauer-Emmett-Teller (BET) analysis was performed on a 3H-2000 automatic specific surface area analyzer with nitrogen adsorption/desorption at 77 K. The structure and composition of the samples were characterized by powder X-ray diffraction (XRD, D-MAX 2200 VPC) and Raman spectra (Renishaw inVia Raman microscope). Cyclic voltammetry (CV) and electronic impedance spectra (EIS) were carried out in a three-electrode cell with an electrolyte of 0.5 M Na_2SO_4 solution using a CHI7601 electrochemical workstation.

2.4 Electrosorption experiments

The homemade electrosorption cell consisted of two acrylic plates, where electrodes with dimensions of 5 cm×5 cm were placed on nickel foams employed as current collectors. Two plastic meshes were placed between the electrodes to provide a gap of 1.0 mm, which was necessary to ensure the flow of electrolyte and prevent short circuits. The cell was sealed with rubber gaskets, and all the components were assembled using nuts and bolts. A potential of 1.5 V was applied to the electrode by either a battery or a solar panel under sunlight irradiation. During desalination, 150 mL of NaCl solution with a concentration of 1000 mg L^{-1} continuously flowed through the system by a peristaltic pump at a constant flow rate (100 mL min^{-1}). The solution conductivity was measured online at the exit of the cell using a conductivity meter (DDS-11A, REX). A schematic diagram of the HCDI system is shown in Figure 4.

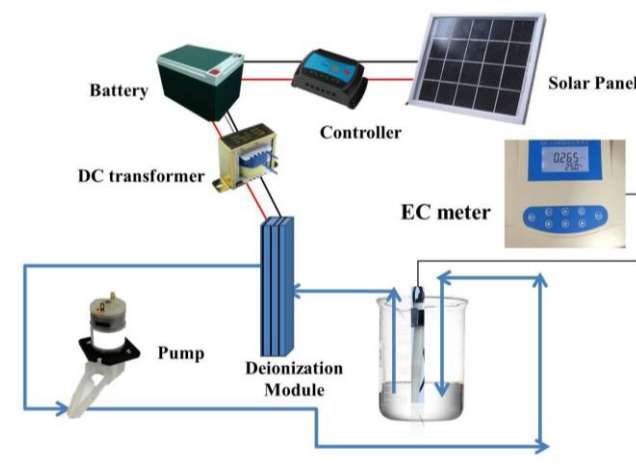


Figure 4. Schematic diagram of the HCEDI system.

The conductivity was converted to a salt concentration according to the correlation between NaCl concentration and electrical conductivity obtained prior to the electrosorption experiment.

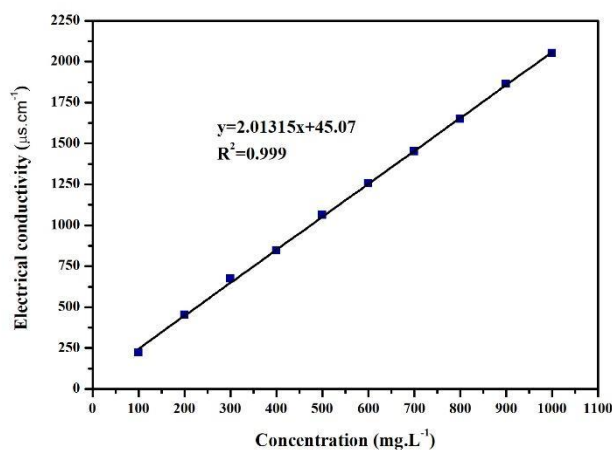


Figure 5. Correlation between NaCl concentration and electrical conductivity at room temperature.

Figure 5 displays a good linear correlation ($R^2 = 0.999$) between the concentration (C) and conductivity (Ec). Eq. (1) is obtained according to Figure 1.

$$C = 0.497 Ec - 22.388 \quad (1)$$

where Ec is the conductivity of the solution, and C is the concentration of the NaCl solution.

Each electrosorption/desorption experiment was performed until no conductivity variation was observed. The salt adsorption capacity (q_s) of the electrodes was calculated according to Eq. (2).

$$q_s = \frac{(C_0 - C_t) \times V}{m} \quad (2)$$

where C_0 (mg L⁻¹) is the initial salt concentration, C_t (mg L⁻¹) is the salt concentration at time t , V (L) is the volume of the electrolyte, and m is the mass of active materials on the cathode and anode (g).

3. RESULTS AND DISCUSSION

3.1 Morphology and Structure of AC

As shown in Figure 6, SEM images of AC samples revealed their porous structure. Figure 6(a) and (b) show the SC-AC particles, with both samples showing that the SC-AC possesses a discontinuous patchy structure. The image of PS-AC (Figure 6(c) and (d)) shows that there are a large number of cavities on the rough surface originating from the dehydrating action of the activating agent. The obvious rough surfaces and a large number of cavities denote a large specific surface area for adsorption. Holes with diameters greater than 1 μm are visible on the PS-AC surfaces.

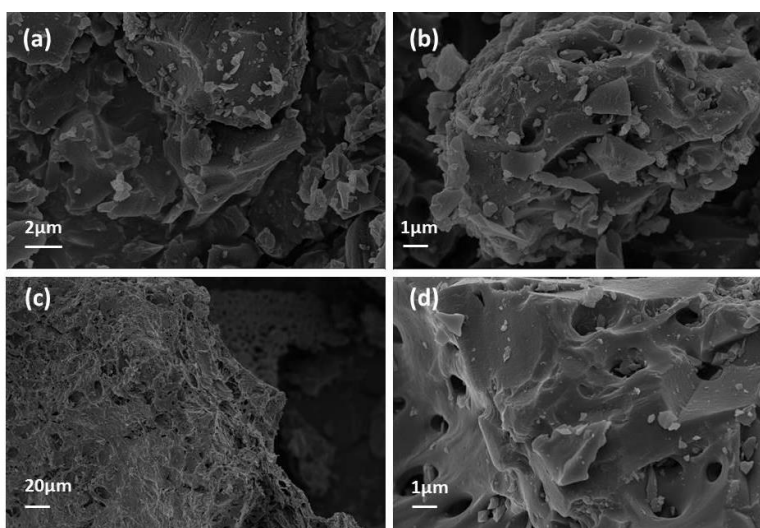


Figure 6. SEM images of the SC-AC (a) (b) and PS-AC (c) (d).

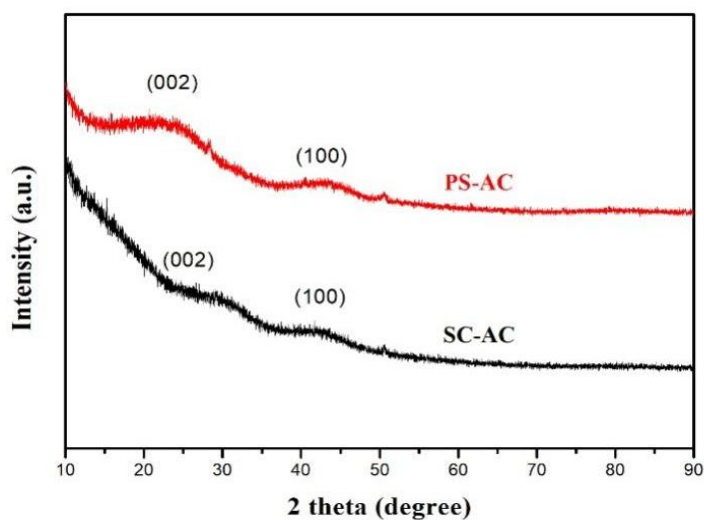


Figure 7. XRD patterns of the PS-AC and SC-AC.

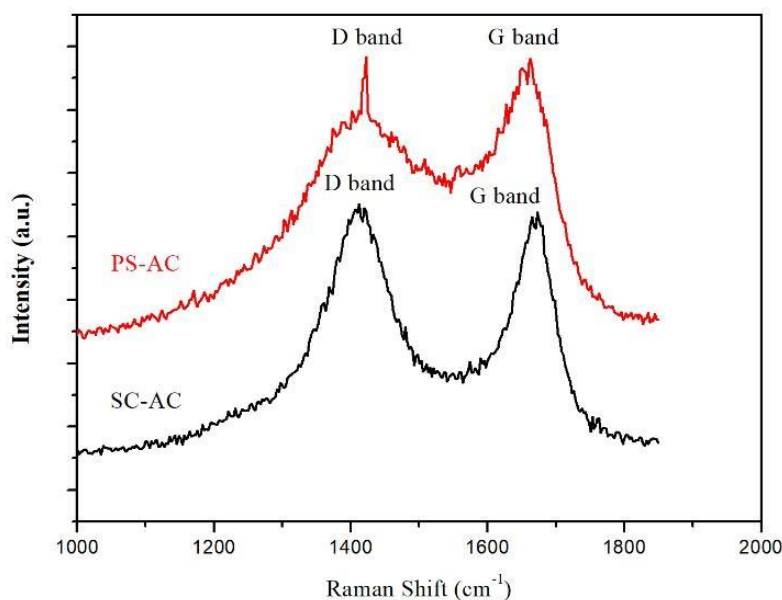


Figure 8. Raman spectra of the PS-AC and SC-AC.

The XRD patterns of PS-AC and SC-AC are shown in Figure 7. Two broad diffraction peaks at 2θ of 24.7° and 43.6° correspond to the (002) planes and (100) planes of the graphitic carbon, respectively (JCPDS No. 75-1621) [45]. The patterns of PS-AC and SC-AC are generally similar, suggesting the amorphous features of two carbon samples. The appearance of a few unidentified peaks may be attributed to the porous structures on the surface.

The Raman spectra of SC-AC and PS-AC, as shown in Figure 8, show the presence of the two bands characteristic of carbon materials. Located at approximately 1340 cm^{-1} is the D band, which is characterized by disordered and defective structures. The band at approximately 1580 cm^{-1} is known as the G band, which is associated with ordered graphite structures that have sp^2 hybridization [46,47].

The BET N_2 adsorption and desorption isotherms of PS-AC are shown in Figure 9. The obtained isotherm exhibits the IUPAC classified-type (I) adsorption isotherm, which is a typical characteristic of microporous materials [48-50]. The BET specific surface area of PS-AC was observed to be $1013.5\text{ m}^2\text{ g}^{-1}$. The curves of the pore size distribution can be found in the inset of Figure 9, which shows a pore size under 2 nm and indicates their presence in the microporous structure. A comparison of the specific surface area and pore size of peanut shell-derived activated carbon in different studies is shown in Table 1. The specific surface area of the PS-AC can be improved by the interaction of various other compounds formed during activation. The larger specific surface area of PS-AC can provide more active sites, which is beneficial to the improvement of the adsorption activity. In theory, only pores with a size of 0.5 nm and above can electrochemically adsorb ions. The adsorption speed is different for different pore sizes; the larger the pores are, the faster the electrochemical adsorption speed [51].

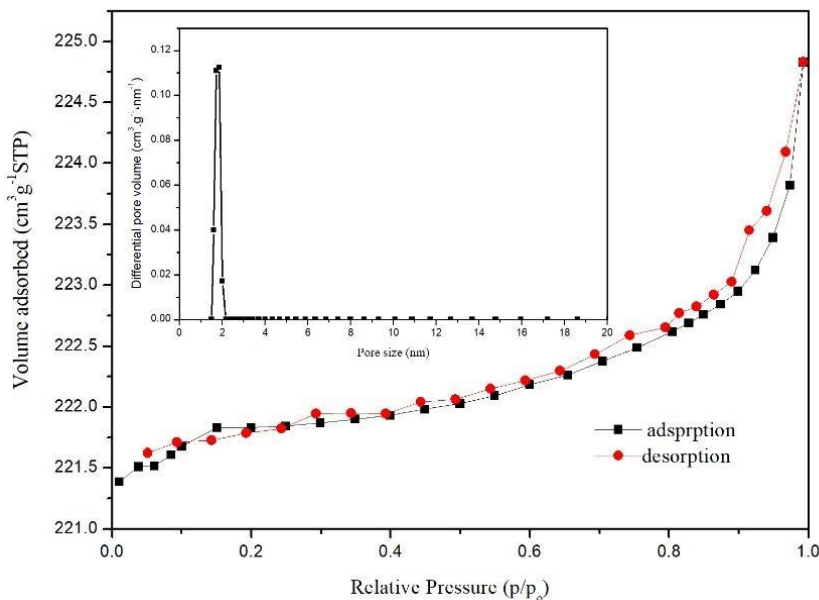


Figure 9. N₂ adsorption-desorption isotherm of the PS-AC (inset: BJH pore distribution of PS-AC).

Table 1. Comparison of BET specific surface area and pore size of peanut shell-derived activated carbons in different literature

Specific surface area (m ² g ⁻¹)	Pore size (nm)	Reference
885~1807	3.40~3.80	[39]
591~1138	1.38~2.34	[52]
956	0.35~0.70	[37]
629~1962	0.30~0.80	[36]
1013.5	1.59~2.34	This work

3.2 Structure and Morphology of Molybdenum Disulfide

SEM images shown in Figure 10(a)(b) and (c)(d) correspond to MoS₂ and D-MoS₂, respectively. It can be seen that the as-prepared spherical molybdenum disulfide material with uniform sizes of approximately 5 μm in diameter show that the spheres are linked together to form larger objects of approximately 10-15 μm in diameter. Further observations revealed that the samples have a nanoflower-like structure assembled from clear nanoflakes, resulting in a large specific surface area. After being thermally treated at 300 °C, the D-MoS₂ presented a similar morphology, as defects are not visible at that scale.

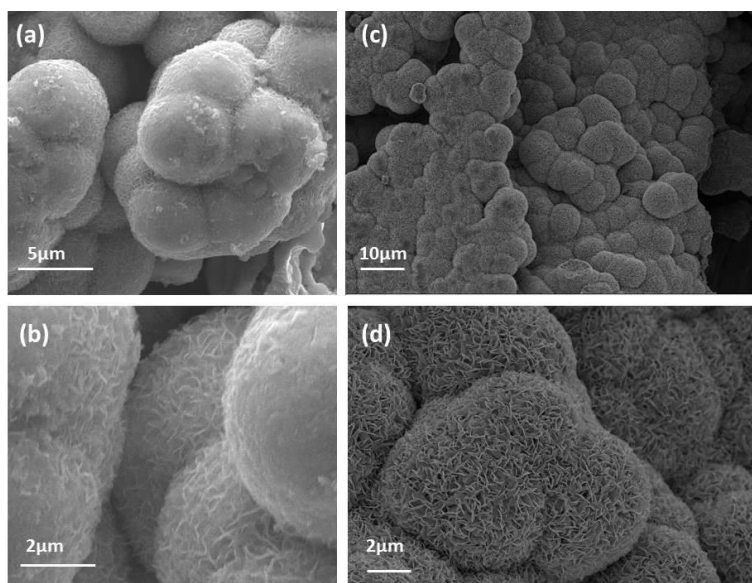


Figure 10. SEM images of the untreated MoS₂ (a) (b) and D-MoS₂ (c) (d).

The obtained sphere-like morphology was further studied using transmission electron microscopy (TEM). The TEM images of the as-prepared D-MoS₂ are shown in Figure 11(a) and (b). The good transparency of these obtained nanoflakes to visible light indicate the general thinness of the nanoflakes, which leads to open and porous three-dimensional structures that are beneficial to electrolyte access and electron transport during electrochemical reactions [53].

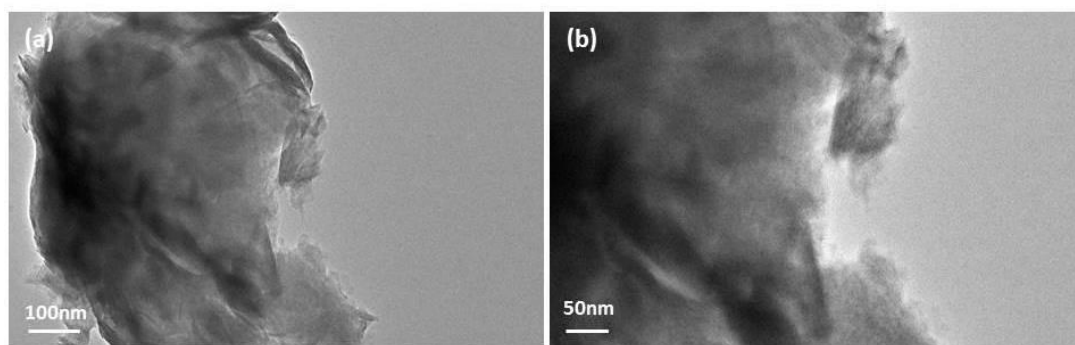


Figure 11. TEM images of D-MoS₂.

The XRD pattern of untreated MoS₂ and D-MoS₂ is illustrated in Figure 12. The distinct diffraction peaks at 2θ of 13.55° , 32.43° , 35.52° , and 57.30° correspond to the primary diffractions of the (002), (100), (103) and (110) planes of MoS₂, agreeing with the hexagonal structure of MoS₂ (JCPDS: 37-1492). This indicates the successful synthesis of MoS₂ with excellent crystallinity. The pattern of D-MoS₂ shows numerous unidentified peaks emerging in the entire range, indicating defects in the crystal plane. This proves the successful introduction of defects on MoS₂ after thermal treatment for 2 hours at 290°C . The Raman spectra of molybdenum disulfide before and after thermal treatment are displayed in Figure 13. Two characteristic peaks at 200 cm^{-1} and 409.4 cm^{-1} were observed for molybdenum

disulfide, which are in line with the in-plane displacement in Mo and S atoms (E_{2g}) and out-plane symmetric displacement of S atoms along the c-axis (A_{1g}), respectively [54].

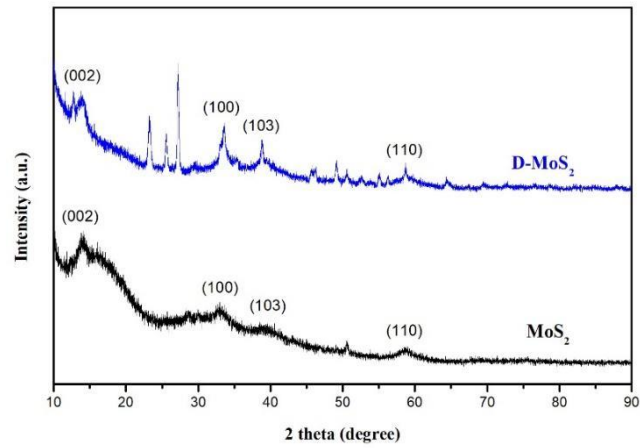


Figure 12. XRD patterns of untreated MoS₂ and D-MoS₂.

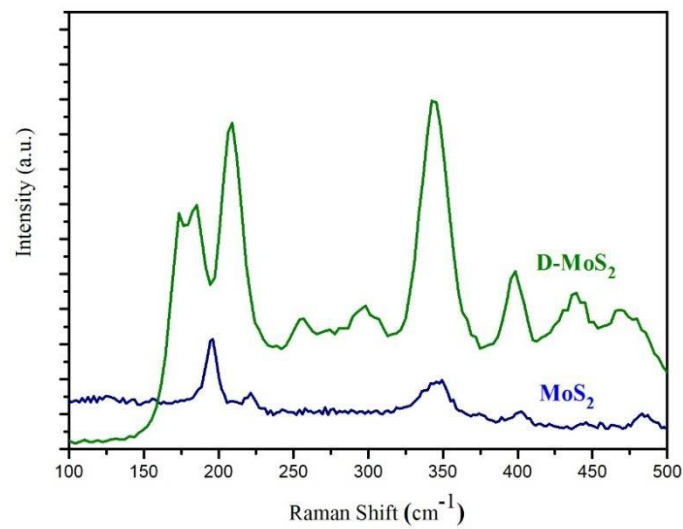


Figure 13. Raman spectra of untreated MoS₂ and D-MoS₂.

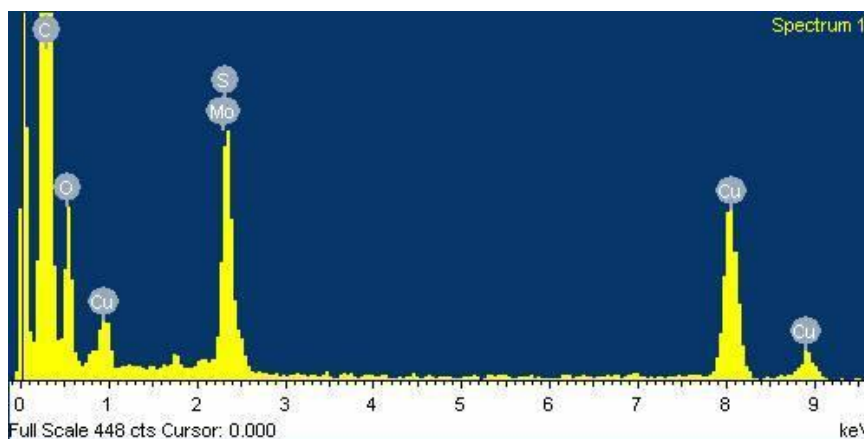


Figure 14. EDS spectra of D-MoS₂.

The chemical composition of D-MoS₂ is further confirmed by EDS analysis as shown in Figure 14. The EDS analysis suggests that the as-prepared MoS₂ materials are composed of mainly Mo and S, proving the purity of the sample after thermal treatment. The element of Cu is the result of the base support.

The nitrogen adsorption-desorption isotherms of D-MoS₂ and MoS₂ exhibited the IUPAC classified-type (IV) adsorption isotherm (Figure 15), which indicates the presence of a mesoporous structure [55]. The special surface area of D-MoS₂ is 16.34 m² g⁻¹ with a pore volume of 0.090 cm³ g⁻¹, which is higher than that of untreated MoS₂ (special surface area of 13.34 m² g⁻¹, pore volume of 0.041 cm³ g⁻¹). Moreover, D-MoS₂ has a wider distribution than untreated MoS₂, and these phenomena may be highly related to the generation of defects during thermal treatment [41], which favors fast ion transport during the charge and discharge process and provides enhanced electrochemical performance [56].

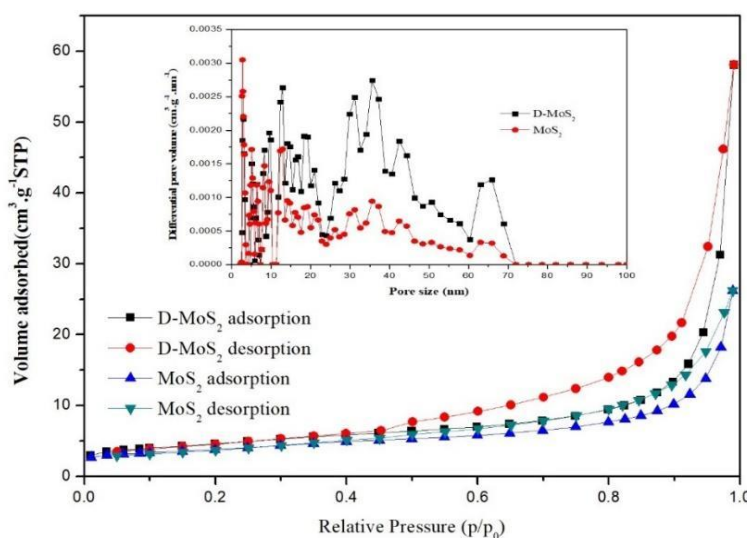


Figure 15. N₂ adsorption-desorption isotherm of the D-MoS₂ and untreated MoS₂ (inset: BJH pore distribution of D-MoS₂ and MoS₂).

3.3 Electrochemical Measurements

The internal resistances of the PS-AC, AC-AC, D-MoS₂ and untreated MoS₂ were determined with an electrochemical impedance spectroscopy (EIS) method. The EIS measurements were carried out on the Ivium Stat electrochemical workstation (Ivium Technologies BV, Netherlands) under open-circuit conditions, with a scanning frequency of 10 000 Hz-0.01 Hz.

Figure 16 shows that the SC-AC and PS-AC curves are different from the typical Nyquist curves, which consist of three parts at different frequencies. This variation can be ascribed to the mixed composition and rough structure of the electrode surface. In the low-frequency region, SC-AC displayed better capacitance performance. The SC-AC curve has a larger slope than the PS-AC curve and is closer to vertical. The more vertical the curve is, the easier it is for the electrolyte ions to approach the surface of the electrodes. Therefore, electrolyte ions can approach the surface of the SC-AC electrode more easily, and it seems that the SC-AC electrode has better capacitor behavior than the others. However, the x-intercept for PS-AC is smaller than that of the SC-AC. As a result, there is less resistance for the PS-AC than for the SC-AC in the high-frequency region, as the x-axis intercept is impedance in the solution [57].

The intercept of the impedance curve on the real axis in the high-frequency region is the equivalent series resistance (ESR), the arc in the low-frequency region indicates the charge transfer resistance (RCT) between the electrode surface and electrolyte [58], as the curve of D-MoS₂ possesses a small x-intercept and a steeper slope, it can be concluded that the D-MoS₂ exhibited superior performance in both regions of high and low frequencies compared to the other samples.

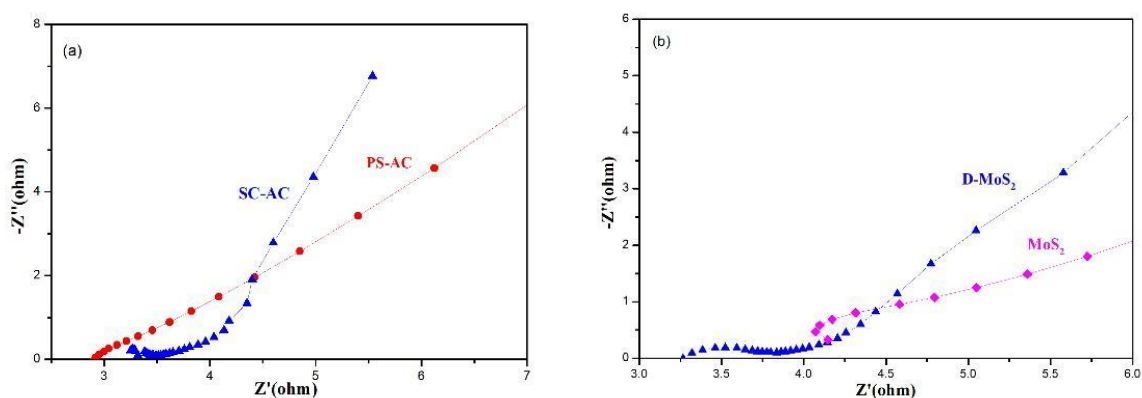


Figure 16. (a) EIS spectra of PS-AC and AC-AC and (b) EIS spectra of D-MoS₂ and untreated MoS₂.

The cyclic voltammogram (CV) is generally used to characterize the capacitive behavior of an electrode material. The cyclical voltammetry curves of the PS-AC, SC-AC, D-MoS₂, and MoS₂ electrodes are measured with a conventional three-electrode system at a 10 mv s⁻¹ scan rate in 1 M NaCl. The results are displayed in Figure 17. No sharp redox peaks are visible for all four curves, which is in good agreement with the typical electric double layer capacitance of the electrodes. This indicates that ions in solution can be adsorbed on the surface of electrodes due to coulombic interactions rather than

electrochemical reactions [59,60]. The specific capacitance value based on the CV plot at various scan rates can be calculated using Eq. (3):

$$C_s = \frac{A}{2m \cdot \Delta V \cdot \nu} \quad (3)$$

where C_s is the specific capacitance of the active material, A is an integral area of the CV loop, ΔV is a potential window, ν is the scan rate and m is the mass of the active material. The specific capacitances of PS-AC, SC-AC, untreated MoS₂ and D-MoS₂ were 87, 91, 91 and 113 F g⁻¹ at a scan rate of 10 mV s⁻¹, respectively.

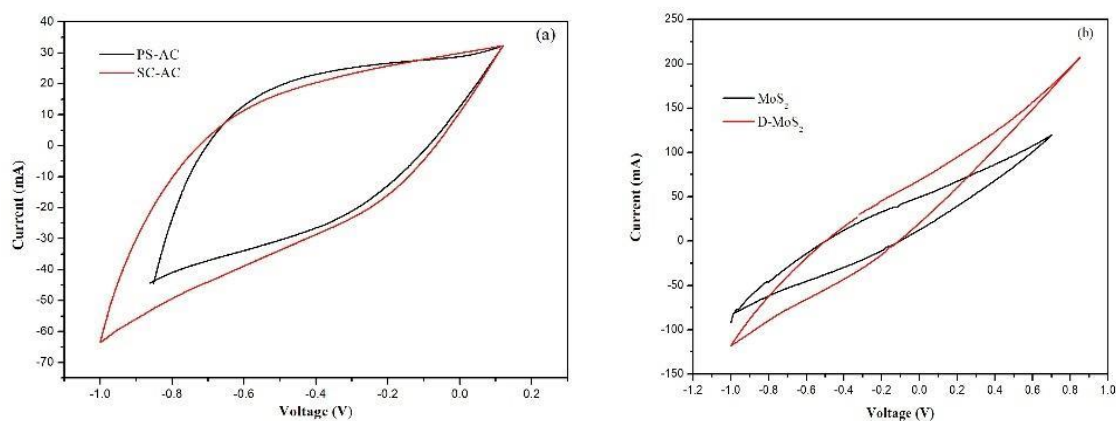


Figure 17. (a) CV curves of the PS-AC and SC-AC and (b) CV curves of the untreated MoS₂ and D-MoS₂.

Table 2. Comparison of specific capacitance for different materials as electrodes

Material	Specific capacitance (F·g ⁻¹)	Reference
palm shell-based AC	33.5	[61]
sawdust-based AC	89	[62]
coffee endocarp-based AC	69	[63]
bamboo-based AC	60	[64]
peanut shell-based AC	87	this work
MoS ₂	74.2	[41]
defect-rich MoS ₂	221.4	[41]
MoS ₂ -carbon nanotube	210	[40]
D-MoS ₂	113	this work

The capacitance of PS-AC is slightly smaller than that of SC-AC, and the capacitance of untreated MoS₂ is also slightly smaller than that of D-MoS₂, which is in line with the BET analysis. The relatively small surface area of PS-AC and untreated MoS₂ agrees with its lower capacitance. This should be addressed by grinding the material thoroughly and exploring better methods of activation treatment.

The specific capacitance is related to the material properties, electrolyte, scan rate and discharge potential, and the specific capacitances of some types of activated carbon (AC) and MoS₂ are shown in Table 2.

3.4 Electrosorption Desalination Performances

Saline water was simulated using NaCl solution in the experiments. The NaCl solution was passed through the cell without an applied voltage until the concentration of NaCl remained essentially unchanged. Previous studies revealed that a high potential triggers redox reactions, and the ideal working potential was determined to be between 1.2 and 1.5 V [65-68]; additionally, a higher cell potential can enhance electrosorption capacity because of the presence of strong electrostatic forces and the formation of a thicker EDL at an increased voltage [69]. Interestingly, an applied voltage above 1.2 V did not result in a greater removal capacity for ions, which is attributed to increased parasitic effects during water electrolysis [26].

In this study, a potential of 1.2 V was applied to the electrodes through a 12 V battery charged using solar energy via a DC transformer. A NaCl solution of 1000 mg L⁻¹ with an electrical conductivity of 2050 $\mu\text{S cm}^{-1}$ flowed through the system for one hour. The electrosorption desalination performances of PS-AC/PS-AC and D-MoS₂/PS-AC combinations are shown in Figure 18. Electrical conductivity decreased at steady rates over the course of the experiment. The PS-AC/SC-AC electrodes displayed a removal rate of 28.7% and the D-MoS₂/PS-AC displayed a rate of 35%.

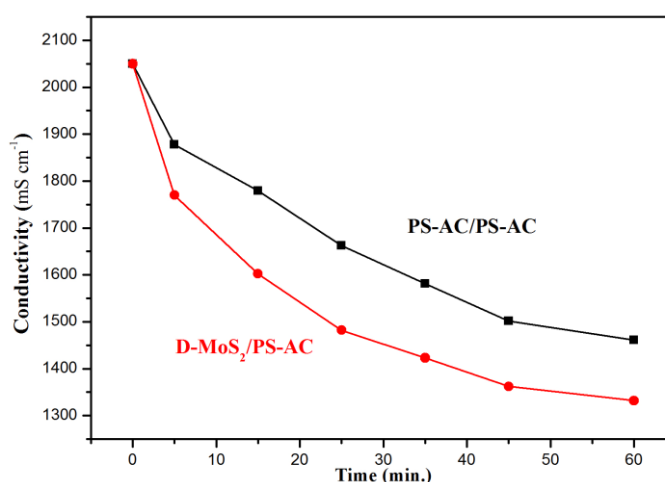


Figure 18. Capacitive deionization performance of the PS-AC/SC-AC and D-MoS₂/PS-AC electrodes. The graph shows the change in concentrations of 1000 mg/L NaCl solution in 60 minutes under 1.2 V.

The electrosorption capacity increases gradually with an increasing initial feeding solution concentration at a constant cell voltage [70]. To investigate the maximum capacitive adsorption capacity of the electrodes, experiments with various initial concentrations of NaCl were conducted. After 60 minutes of desalination, the electrosorption capacity was calculated for each run employing Eq. (2). As shown in Figure 19, the specific salt-adsorption capacity increases with increasing solution concentration. For 1000 mg L⁻¹ of initial NaCl, the maximum specific salt-adsorption capacity of the D-MoS₂/PS-AC system was approximately 8.98 mg g⁻¹, which is higher than that of the PS-AC/PS-AC system.

The results from Figure 19 confirm that the D-MoS₂ electrode achieves a higher electrosorption desalination ratio. The MoS₂-based electrodes possess higher electrosorption capacity because MoS₂ has a negatively charged surface, which attracts more ions due to coulombic interaction [40].

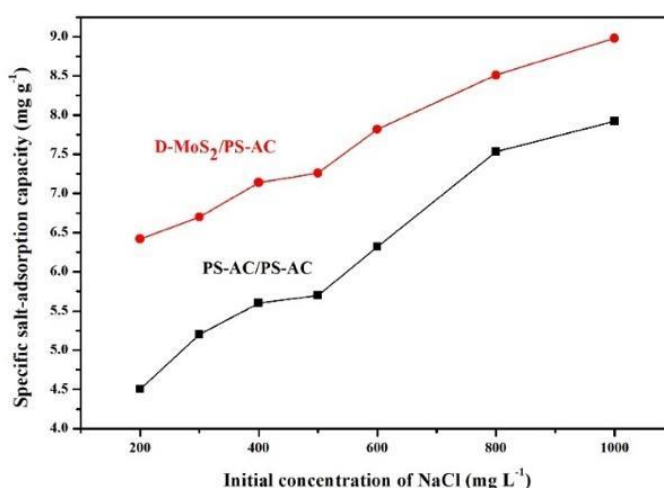


Figure 19. Electrosorption capacity of the electrodes at various initial concentrations of NaCl. Electrosorption capacities are calculated by exploring the change in concentrations of 200, 300, 400, 500, 600, 800, and 1000 mg/L NaCl solution in 60 minutes under 1.2 V.

A comparison of the electrosorption capacities of different electrode materials is summarized in Table 3. Compared to the other electrode materials listed in Table 3, the PS-AC electrodes showed higher electrosorption capacities than the AC electrodes, indicating the superiority of biomass materials and their immense potential.

The regeneration property of the electrodes is one of the distinctive attributes of capacitive deionization. Figure 20 shows that the CDI performances of the samples are stable in multiple cycles, and electrodes can be reused by adjusting the voltage to 0.0 V or reversing the applied voltage, which causes ion desorption. A NaCl solution of 300 mg L⁻¹ was used to study the adsorption-desorption capabilities. Figure 20 illustrates that the electrosorption capacity did not decrease after 4 cycles. Additionally, the D-MoS₂/PS-AC electrodes possess not only a high capacity but also a short cycle period for deionization. Thus, using the D-MoS₂/PS-AC as the electrode material, the electrosorption/electrodesorption process may be both fast and repeatable.

Table 3. Comparison of electrosorption capacity for some electrode materials

Material	Initial concentration of NaCl (mg L^{-1})	Applied voltage (V)	Electrosorption capacity (mg g^{-1})	Reference
Activated carbon	1000	1.2 V	7.12	[71]
Carbon aerogel	500	1.2	5.62	[72]
T-MoS ₂	100	0.8	24.6	[41]
PS-AC	1000	1.5 V	7.92	This study
D-MoS ₂ /PS-AC	1000	1.5 V	8.98	This study

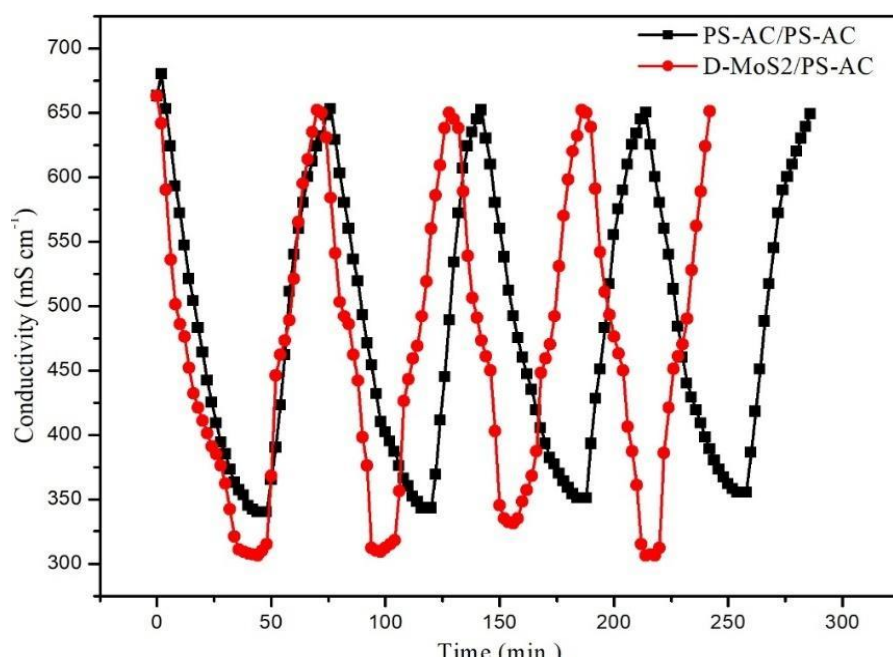


Figure 20. Cyclic adsorption/desorption performance of the PS-AC/PS-AC and D-MoS₂/PS-AC electrodes. The test was conducted using 300 mg/L NaCl solution. The voltage for the adsorption process is 1.2 V, while that of the desorption process is 0.0 V

4. CONCLUSION

In this work, peanut shells were used to prepare activated carbon, while defects were introduced to MoS₂ through thermal treatment. CDI performances were tested to obtain electrosorption capacities of 7.92 mg/g and 8.98 mg/g for the PS-AC/PS-AC and D-MoS₂/PS-AC electrodes, respectively. Characterization results revealed the enhanced performance of D-MoS₂ originating from the lowering of impedance due to the introduction of defects and the large pore width of PS-AC. The surface area of PS-AC could be further improved by exploring better ways for the activation process. As the possibility of

using solar power for HCDI was also validated during experiments, the study has prospects of being applied in resolving water crises in arid coastal and island regions worldwide.

ACKNOWLEDGEMENTS

This project is supported financially by the Talent Program of Children & Youth Science Center (CYSC) that is affiliated with the China Association for Science and Technology (CAST). The authors are sincerely thankful for the kind help of Prof. Ye Xiang Tong from Sun Yat-Sen University and Dr. Yong Chao Huang from Guangzhou University.

References

1. M.M. Mekonnen, A.Y. Hoekstra, *Science Advances*, 2 (2016) 1.
2. I. Shiklomanov, *Water in Crisis: A Guide to the World's Fresh Water Resources*, Oxford University Press, New York, 1993.
3. N. Shekarchi, F. Shahnia, *International Journal of Energy Research*, 43 (2019) 1357.
4. M. Elimelech, W.A. Phillip, *Science*, 333 (2011) 712.
5. M.A. Shannon, P.W. Bohn, M. Elimelech, J.G. Georgiadis, B.J. Marinas, A.M. Mayes, *Nature*, 452 (2008) 301.
6. R.F. Service, *Science*, 313 (2006) 1088.
7. M.G. Ahunbay, *Desalination*, 465 (2019) 58.
8. J. Lee, P. Srimuk, R.L. Zornitta, M. Aslan, B.L. Mehdi, V. Presser, *Acs Sustainable Chemistry & Engineering*, 7 (2019) 10132.
9. G. Divyapriya, K.K. Vijayakumar, I. Nambi, *Desalination*, 451 (2019) 102.
10. P. Srimuk, et al., *Electrochimica Acta*, 224 (2017) 314.
11. S. Porada, A. Shrivastava, P. Bukowska, P.M. Biesheuvel, K.C. Smith, *Electrochimica Acta*, 255 (2017) 369.
12. J. Lee, P. Srimuk, K. Aristizabal, C. Kim, S. Choudhury, Y.-C. Nah, F. Mucklich, V. Presser, *Chemsuschem*, 10 (2017) 3611.
13. J. Choi, Y. Oh, S. Chae, S. Hong, *Desalination*, 462 (2019) 19.
14. M.E. Suss, S. Porada, X. Sun, P.M. Biesheuvel, J. Yoon, V. Presser, *Energy & Environmental Science*, 8 (2015) 2296.
15. S. Porada, R. Zhao, A. van der Wal, V. Presser, P.M. Biesheuvel, *Progress in Materials Science*, 58 (2013) 1388.
16. L. Zou, L. Li, H. Song, G. Morris, *Water Research*, 42 (2008) 2340.
17. A.S. Yasin, I.M.A. Mohamed, M.T. Amen, N.A.M. Barakat, C.H. Park, C.S. Kim, *Journal of Alloys and Compounds*, 772 (2019) 1079.
18. L. Guo, X. Wang, Z.Y. Leong, R. Mo, L. Sun, H.Y. Yang, *Flatchem*, 8 (2018) 17.
19. P. Liang, L. Yuan, X. Yang, S. Zhou, X. Huang, *Water Research*, 47 (2013) 2523.
20. G. Li, W. Cai, R. Zhao, L. Hao, *Environmental Science and Pollution Research*, 26 (2019) 17787.
21. C. Tan, C. He, W. Tang, P. Kovalsky, J. Fletcher, T.D. Waite, *Water Research*, 147 (2018) 276.
22. P.A. Fritz, F.K. Zisopoulos, S. Verheggen, K. Schroen, R.M. Boom, *Desalination*, 444 (2018) 162.
23. H. Li, L. Zou, *Desalination*, 275 (2011) 62.
24. K.H. Kim, D.H. Kang, M.J. Kim, Y.-S. Lee, *Desalination*, 457 (2019) 1.
25. R.L. Zornitta, F.J. Garcia-Mateos, J.J. Lado, J. Rodriguez-Mirasol, T. Cordero, P. Hammer, L.A.M. Ruotolo, *Carbon*, 123 (2017) 318.
26. W. Huang, Y. Zhang, S. Bao, R. Cruz, S. Song, *Desalination*, 340 (2014) 67.

27. H. Wan, X. Hu, *Chemical Physics*, 521 (2019) 108.
28. S. Sankar, S. Saravanan, A.T.A. Ahmed, A.I. Inamdar, H. Im, S. Lee, D.Y. Kim, *Materials Letters*, 240 (2019) 189.
29. M. Baysal, K. Bilge, B. Yilmaz, M. Papila, Y. Yurum, *Journal of Environmental Chemical Engineering*, 6 (2018) 1702.
30. D. Momodu, A. Bello, K. Oyedotun, F. Ochai-Ejeh, J. Dangbegnon, M. Madito, N. Manyala, *Rsc Advances*, 7 (2017) 37286.
31. A.H. Jawad, R. Abd Rashid, M.A.M. Ishak, L.D. Wilson, *Desalination and Water Treatment*, 57 (2016) 25194.
32. A.M. Abioye, F.N. Ani, *Renewable & Sustainable Energy Reviews*, 52 (2015) 1282.
33. L. Tao, H. Chen, J. Liu, S. Zhang, *Environmental Pollution & Control*, 40 (2018) 639.
34. W. Cai, Z. Li, J. Wei, Y. Liu, *Chemical Engineering Research & Design*, 140 (2018) 23.
35. A. Ariharan, B. Viswanathan, *Indian Journal of Chemical Technology*, 25 (2018) 140.
36. K. Lewicka, *Polish Journal of Chemical Technology*, 19 (2017) 38.
37. S. Deng, B. Hu, T. Chen, B. Wang, J. Huang, Y. Wang, G. Yu, *Adsorption-Journal of the International Adsorption Society*, 21 (2015) 125.
38. J. Ding, H. Wang, Z. Li, K. Cui, D. Karpuzov, X. Tan, A. Kohandehghan, D. Mitlin, *Energy & Environmental Science*, 8 (2015) 941.
39. J. Liu, Y. Liu, J. Peng, Z. Liu, Y. Jiang, M. Meng, W. Zhang, L. Ni, *Water Air and Soil Pollution*, 229 (2018) 391.
40. P. Srimuk, J. Lee, S. Fleischmann, S. Choudhury, N. Jaeckel, M. Zeiger, C. Kim, M. Aslan, V. Presser, *Journal of Materials Chemistry A*, 5 (2017) 15640.
41. F. Jia, K. Sun, B. Yang, X. Zhang, Q. Wang, S. Song, *Desalination*, 446 (2018) 21.
42. X. Zhang, Z. Lai, C. Tan, H. Zhang, *Angewandte Chemie-International Edition*, 55 (2016) 8816.
43. E.G. da Silveira Firmiano, A.C. Rabelo, C.J. Dalmaschio, A.N. Pinheiro, E.C. Pereira, W.H. Schreiner, E.R. Leite, *Advanced Energy Materials*, 4 (2014) 1301380.
44. G. Zhang, H. Liu, J. Qu, J. Li, *Energy & Environmental Science*, 9 (2016) 1190.
45. J. Hou, C. Cao, F. Idrees, X. Ma, *Acs Nano*, 9 (2015) 2556.
46. A. Ghosh, A.M. da Silva Santos, J.R. Cunha, A. Dasgupta, K. Fujisawa, O.P. Ferreira, A.O. Lobo, M. Terrones, H. Terrones, B.C. Viana, *Vibrational Spectroscopy*, 98 (2018) 111.
47. F.C.C. Moura, R.D.F. Rios, B.R.L. Galvao, *Environmental Science and Pollution Research*, 25 (2018) 26482.
48. H. Demiral, I. Demiral, *Surface and Interface Analysis*, 40 (2008) 612.
49. S. Sun, Q. Yu, M. Li, H. Zhao, C. Wu, *Renewable Energy*, 142 (2019) 11.
50. K.R.A. Saravanan, N. Prabu, M. Sasidharan, G. Maduraiveeran, *Applied Surface Science*, 489 (2019) 725.
51. H.S. Deyang Qu *Journal of Power Sources*, 74 (1998) 99.
52. H. Wu, R. Chen, H. Du, J. Zhang, L. Shi, Y. Qin, L. Yue, J. Wang, *Adsorption Science & Technology*, 37 (2019) 34.
53. F. Wang, G. Li, J. Zheng, J. Ma, C. Yang, Q. Wang, *Rsc Advances*, 8 (2018) 38945.
54. C. Lee, H. Yan, L.E. Brus, T.F. Heinz, J. Hone, S. Ryu, *Acs Nano*, 4 (2010) 2695.
55. M. Chen, J. Wang, X. Yan, J. Ren, Y. Dai, Q. Wang, Y. Wang, X. Cheng, *Journal of Alloys and Compounds*, 722 (2017) 250.
56. B. Liu, P. Soares, C. Checkles, Y. Zhao, G. Yu, *Nano Letters*, 13 (2013) 3414.
57. H.K. Song, H.Y. Hwang, K.H. Lee, L.H. Dao, *Electrochimica Acta*, 45 (2000) 2241.
58. D.N.Sangeetha, M.Selvakumar, *Applied Surface Science*, 453(2018) 132.
59. M.W. Ryoo, J.H. Kim, G. Seo, *J. Colloid Interface Sci.*, 264(2003) 414.
60. X. Quan, Z. Fu, L. Yuan, M. Zhong, R. Mi, X. Yang, Y. Yi, C. Wang, *Rsc Advances*, 7 (2017) 35875.
61. P. -A. Chen, H-C. Cheng, H. Paul Wang, *Journal of Cleaner Production*, 174 (2018) 927.

62. Wu-Jun Liu , Ke Tian , Yan-Rong He , Hong Jiang, Han-Qing Yu, *Environmental science & technology*,48(2014)13951.
63. J.M Valenten Nabais, JG Teixeira, I Almeida, *Bioresource Technology*, 102(2011)2781.
64. C. Kim, J. Lee, J. Kim, *Korean journal of chemical Engineering*, 23(2006)592.
65. S. Porada, R. Zhao, A. van der Wal, V. Presser and P. M.Biesheuvel, *Progress Material Science*, 58(2013)1388.
66. S. Porada, L. Borchardt, M. Oschatz, M. Bryjak, J. S. Atchison, K. J. Keesman, S. Kaskel, P. M. Biesheuvel and V.Presser, *Energy Environment Science*, 6(2013)3700.
67. H. Li, L. Zou, L. Pan and Z. Sun, *Separation Purification Technology*, 75(2010)8.
68. C. Tsouris, R. Mayes, J. Kiggans, K. Sharma, S. Yiacoumi, D. DePaoli and S. Dai, *Environment Science Technology*, 45(2011)10243.
69. D. Sriramulu, S. Vafakhah and H. Y. Yang, *RSC Advances*, 9(2019)14884.
70. Z. Huang, M. Wang, L. Wang, and F. Kang, *Langmuir*, 28(2012)5079.
71. H. Bi, B. Tian, *Chinese Journal of Environmental Engineering*, 9 (2015) 1606.
72. X. Quan, Z. Fu, L. Yuan, M. Zhong, R. Mi, X. Yang, Y. Yi, C. Wang, *Rsc Advances*, 7 (2017) 35875.

© 2020 The Authors. Published by ESG (www.electrochemsci.org). This article is an open access article distributed under the terms and conditions of the Creative Commons Attribution license (<http://creativecommons.org/licenses/by/4.0/>).